



## RESEARCH ARTICLE

10.1002/2015WR018254

# Pore-scale displacement mechanisms as a source of hysteresis for two-phase flow in porous media

S. Schlüter<sup>1,2</sup>, S. Berg<sup>3</sup>, M. Rücker<sup>3,4</sup>, R. T. Armstrong<sup>5</sup>, H.-J. Vogel<sup>1,6</sup>, R. Hilfer<sup>7</sup>, and D. Wildenschild<sup>2</sup>

### Key Points:

- Real-time fluid displacement analysis with fast synchrotron-based X-ray tomography
- Changes in fluid topology are characteristic for the underlying displacement mechanisms
- Fluid topology correlates well with fluid trapping

### Supporting Information:

- Supporting Information S1
- Movie S1
- Movie S2
- Movie S3

### Correspondence to:

S. Schlüter,  
steffen.schlueter@ufz.de

### Citation:

Schlüter, S., S. Berg, M. Rücker, R. T. Armstrong, H.-J. Vogel, R. Hilfer, and D. Wildenschild (2016), Pore-scale displacement mechanisms as a source of hysteresis for two-phase flow in porous media, *Water Resour. Res.*, 52, 2194–2205, doi:10.1002/2015WR018254.

Received 16 OCT 2015

Accepted 26 FEB 2016

Accepted article online 4 MAR 2016

Published online 24 MAR 2016

<sup>1</sup>Department of Soil Physics, Helmholtz-Centre for Environmental Research - UFZ, Halle, Germany, <sup>2</sup>School of Chemical, Biological and Environmental Engineering, Oregon State University, Corvallis, Oregon, USA, <sup>3</sup>Shell Global Solutions International B.V., Rijswijk, Netherlands, <sup>4</sup>Department of Earth Science & Engineering, Imperial College London, London, UK, <sup>5</sup>School of Petroleum Engineering, University of New South Wales, Sydney, Australia, <sup>6</sup>Institut für Agrar- und Ernährungswissenschaften, Martin-Luther-Universität Halle-Wittenberg, Halle, Germany, <sup>7</sup>Institut für Computerphysik, Universität Stuttgart, Stuttgart, Germany

**Abstract** The macroscopic description of the hysteretic behavior of two-phase flow in porous media remains a challenge. It is not obvious how to represent the underlying pore-scale processes at the Darcy-scale in a consistent way. Darcy-scale thermodynamic models do not completely eliminate hysteresis and our findings indicate that the shape of displacement fronts is an additional source of hysteresis that has not been considered before. This is a shortcoming because effective process behavior such as trapping efficiency of CO<sub>2</sub> or oil production during water flooding are directly linked to pore-scale displacement mechanisms with very different front shape such as capillary fingering, flat frontal displacement, or cluster growth. Here we introduce fluid topology, expressed by the Euler characteristic of the nonwetting phase ( $\chi_n$ ), as a shape measure of displacement fronts. Using two high-quality data sets obtained by fast X-ray tomography, we show that  $\chi_n$  is hysteretic between drainage and imbibition and characteristic for the underlying displacement pattern. In a more physical sense, the Euler characteristic can be interpreted as a parameter describing local fluid connectedness. It may provide the closing link between a topological characterization and macroscopic formulations of two-phase immiscible displacement in porous rock. Since fast X-ray tomography is currently becoming a mature technique, we expect a significant growth in high-quality data sets of real time fluid displacement processes in the future. The novel measures of fluid topology presented here have the potential to become standard metrics needed to fully explore them.

## 1. Introduction

Immiscible, two-phase fluid flow in porous media is ubiquitous in nature and industrial applications and involves such diverse processes as carbon sequestration, enhanced oil recovery, groundwater remediation, or fluid separation in fuel cells. The phase distribution of these fluids during flow depends on the inherent architecture of the pore space, on the wettability of the solid phase as well as on the external hydraulic forcing. Changing the relative importance of gravity, capillary, and viscous forces results in a rich variety of macroscopic displacement patterns that are typically classified in phase diagrams of flow regimes [Lenormand *et al.*, 1988; Hughes and Blunt, 2000; Herring *et al.*, 2015].

The question about the complete set of Darcy-scale state variables to model macroscopic fluid displacement is a long-standing problem. These macroscopic state variables need to account for the complexity of fluid configurations at the pore scale and at the same time be measurable at the scale of observation to build a useful model. In almost all practical applications, this limitation reduces the set of state variables to the macroscopic capillary pressure ( $P_c$ ), i.e., the pressure difference between two fluids in hydrostatic equilibrium, as a function of wetting fluid saturation ( $S_w$ ) [Bear, 1972; Dullien, 1992]. It is evident that a simple volume density cannot differentiate between different displacement patterns. This oversimplification causes hysteresis and dynamic effects in the  $P_c(S_w)$ -relationship, i.e., it has different curves for drainage and imbibition and depends on the rate of  $S_w$  change.

A practical solution to this nonuniqueness problem are empirical model extensions that reproduce these effects but leave the question of missing state variables unaddressed. The importance of  $A_{wn}$  in this respect

was pointed out by numerous authors [Marle, 1982; Hassanizadeh and Gray, 1993; Hilfer, 1998; Hilfer and Besserer, 2000; Niessner and Hassanizadeh, 2008; Joekar-Niasar et al., 2008]. But the closure problem for the additional unknown field has remained unsolved. Moreover, recent studies with numerical pore network models [Joekar-Niasar and Hassanizadeh, 2012] and etched micromodels [Karadimitriou et al., 2014] have demonstrated that the  $P_c(S_w, A_{wn})$ -relationship is in fact also hysteretic, when a significant amount of fluid volume becomes disconnected. The authors also state that in the underlying thermodynamic theory biconnectivity of fluid phases is assumed—a condition which is not always met under natural conditions.

In this paper, we provide an alternative approach to identify other missing state variables based on integral geometry. This approach is motivated by the fact that differences in displacement patterns at the pore scale are the actual cause for capillary pressure hysteresis and that bulk volumes and interface density only provide indirect information on the underlying fluid displacement process. These processes are rather described by the shape of the displacement front and the change in fluid connectivity through interfacial jumps, snap-off and other pore-scale processes [Berg et al., 2013; Krummel et al., 2013; Pak et al., 2015]. This raises the question whether process-dependent fluid connectivity represents an additional source for hysteresis of macroscopic state variables [Hilfer, 2006]. Fluid connectivity has recently gained interest in the analysis of capillary trapping during water flooding. Fluid topology prior to water flooding, i.e., the degree of connectedness through redundant pathways in the nonwetting phase, was shown to be a key parameter for trapping efficiency [Herring et al., 2013, 2015]. Moreover, this nonwetting phase topology during water flooding is strongly correlated with relative permeability, which changes drastically at the transition from a connected pathway and film swelling regime to a disconnected ganglion dynamics regime [Rücker et al., 2015a].

The objective of this study is therefore to extend the set of conventional, macroscopic state variables by the Euler characteristic as a measure of fluid topology. It will be shown that the Euler characteristic carries complementary information on displacement patterns that is able to explain hysteresis in interfacial area between drainage and imbibition. Moreover, we demonstrate a close relationship between the Euler characteristic and percolation properties. This will be demonstrated by studying the phase distribution of a wetting (brine) and nonwetting fluid (dodecane) during a complete drainage and imbibition cycle in a sintered glass bead packing at very low flow rates. Since the generalization of findings from such a simplified porous medium to more natural porous media is always questionable, we will underpin them with a fractional flow experiment (brine and decane) performed with a porous medium that resembles a natural sandstone. The fluid displacement in both experiments is monitored with fast, synchrotron-based X-ray microtomography which allows for continuous pumping during image acquisition.

## 2. Methods

### 2.1. Quasistatic Drainage and Imbibition

The quasistatic flow experiment was conducted with sintered soda lime beads in a cylindrical quartz glass container (porosity 33%, 5.8 mm diameter, 7.3 mm height). Brine (1:6 mass ratio between CsCl and water) was used as the wetting fluid and n-dodecane as the nonwetting fluid. The bottom of the sample was connected to a syringe pump filled with brine. The top of the sample was connected to a dodecane reservoir at atmospheric pressure. We ran a full cycle of primary drainage (PD), main imbibition (MI), and main drainage (MD) at very slow flow rates. The capillary number, i.e., the ratio between viscous forces and capillary forces [Dullien, 1992], was  $Ca = 10^{-8}$ , so the fluids always remained close to hydraulic equilibrium. The experimental setup is explained in detail in supporting information, **S1**. Fluid distributions were monitored with fast synchrotron-based X-ray tomography at the GSECARS beam line of the Advanced Photon Source (APS) at the Argonne National Laboratory, Argonne, IL, USA, with a spatial resolution of 8.4  $\mu\text{m}$  and a temporal resolution of 113 s. Very accurate segmentation results were achieved with an image processing work flow that was particularly developed for this study (supporting information, **S1**). The field of view (128  $\text{mm}^3$ ) covers a representative elementary volume (REV) in terms of water retention (supporting information, **S2**). In general, the REV is a process-dependent concept. For two-phase flow, the critical length of the sample is governed by the maximum size of fluid clusters, which differs with flow rate [Armstrong et al., 2014; Hilfer and Øren, 1996]. It is likely, that this REV is not reached for all investigated flow regimes. This is a fundamental problem of synchrotron-based X-ray tomography, where the field of view is constrained by the cross-sectional

area of the beam. The consequence will be briefly discussed for the findings that might be biased by the small sample size.

## 2.2. Fractional Flow

The fractional flow experiment was conducted with a strongly water-wet, sintered Robuglas<sup>®</sup> sample (porosity 33%, permeability  $22 \pm 2$  D, 4 mm diameter, 20 mm height). The sample is similar to a strongly water-wet sandstone both in terms of pore-size distribution and long-range connectivity of the wetting fluid [Berg *et al.*, 2014]. Brine (1:6 mass ratio between CsCl and water) was used as the wetting phase and n-decane as the nonwetting phase. The sample was mounted onto a flow cell with two remotely controlled micro piston pumps to allow coinjection of two fluids. Images of fluid distributions were acquired with fast, synchrotron-based X-ray tomography (TOMCAT beam line, Paul Scherrer Institute, Villigen, Switzerland) at a spatial resolution of 2.2  $\mu\text{m}$  and a temporal resolution of 60 s. More information about the experimental setup and image processing steps can be retrieved from supporting information, S1 Methods.

## 2.3. Morphological Descriptors of Phase Distribution

Integral geometry provides a set of morphological descriptors denoted as Minkowski functionals [Mecke, 2000; Ohser and Mücklich, 2000; Vogel *et al.*, 2010] (quermassintegrals, intrinsic volumes) which provide information on content, area, curvature, and topology of spatial structures. Minkowski functionals are defined for binary structures. So far they have mainly been applied to pore structures in order to estimate hydraulic properties [Mecke and Arns, 2005; Lehmann *et al.*, 2008]. Here we extend this to a three-phase system, where one fluid phase is considered as foreground, while the other fluid phase and the solid phase constitute the background. In 3-D, there are four Minkowski functionals ( $M_{0-3}$ ) which all describe different aspects of phase distribution:  $M_0$ —Volume [ $L^3$ ],  $M_1$ —Surface Area [ $L^2$ ],  $M_2$ —Integrated Mean Curvature [ $L$ ], and  $M_3$ —Integrated Gaussian Curvature. Hadwiger's completeness theorem [Hadwiger, 1957] states that every motion-invariant, conditional continuous and additive functional in three dimensions, such as thermodynamic potentials [Mecke and Arns, 2005], can be written as a linear combination of these four Minkowski functionals. While the conventional, macroscopic state variables  $S_{wr}$ ,  $A_{wnr}$ , and  $P_c$  relate to  $M_{0-2}$ , integrated Gaussian curvature is not represented in macroscopic two-phase flow descriptions so far. This dimensionless number is related to the Euler characteristic, which is a topological measure that describes connectedness of a phase by counting fluid clusters and inherent loops. The Euler characteristic for the wetting phase ( $\chi_w$ ) and for the nonwetting phase ( $\chi_n$ ) are independent measures and have to be reported separately. The following relation applies:

$$\chi = \frac{M_3}{4\pi} = \mathcal{N} - \mathcal{L} + \mathcal{O}, \quad (1)$$

where  $\chi$  is the Euler characteristic,  $\mathcal{N}$  is the number of isolated clusters of a fluid phase,  $\mathcal{L}$  is the number of redundant connections within all clusters, and  $\mathcal{O}$  is the number of cavities, e.g., isolated background clusters completely enclosed by the phase of interest. Cavities would only exist, if nonwetting phase was separated from the continuous solid phase through wetting films thicker than the image resolution (8.4 and 2.2  $\mu\text{m}$ ). Therefore,  $\mathcal{O}$  can be neglected for both fluids over the whole range of saturations. The schematic in Figure 1a demonstrates how different displacement regimes such as capillary fingering during drainage and cluster growth during imbibition evoke different  $\chi_n$ , while other state variables are equal. Similar to saturation,  $S_{wr}$ , and interface density,  $A_{wnr}$ , it is convenient to normalize  $\chi$  with total volume to describe it as a density in physical units [ $L^{-3}$ ].

## 3. Results

### 3.1. Quasistatic Drainage and Imbibition

We analyze displacement patterns at the pore scale during drainage and imbibition to elucidate the origin of hysteresis. A key question is to understand how and why exactly drainage and imbibition processes lead to differences in pore-scale fluid configurations. Therefore, the change of standard macroscopic state variables ( $P_c$ ,  $S_{wr}$ ,  $A_{wnr}$ ) and the Euler characteristic ( $\chi_w$ ,  $\chi_n$ ) are monitored during flux-controlled two-phase flow (brine and dodecane) in a sintered glass beads sample for a cycle of primary drainage (PD), main imbibition (MI), and main drainage (MD). Snapshots of phase distributions during primary drainage and main

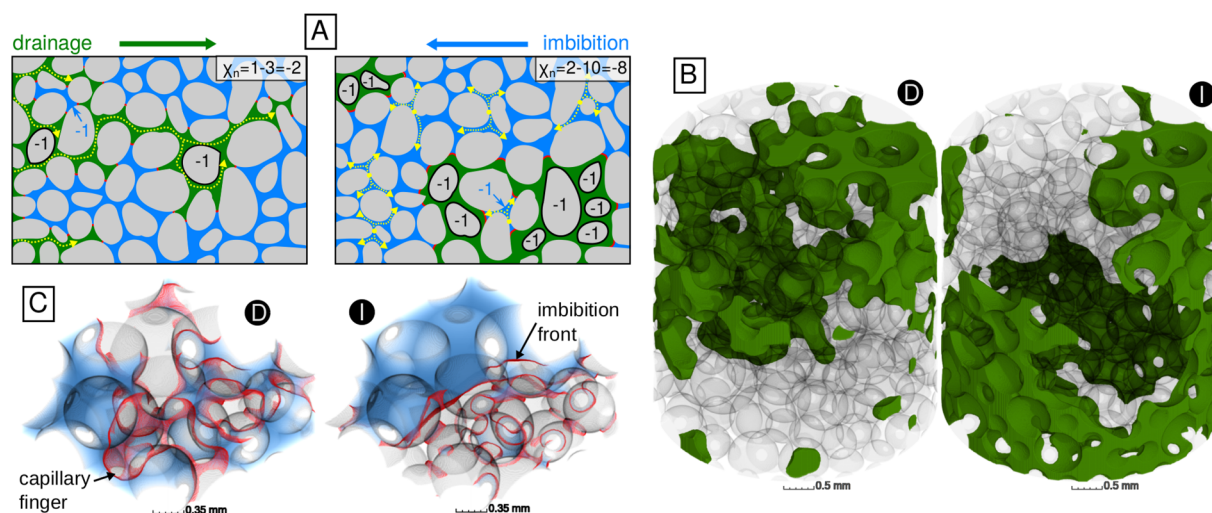


**Figure 1.** (a) Schematic on the relationship between displacement mechanism and the Euler characteristic of the nonwetting phase  $\chi_n$ . During drainage, capillary fingers may form (yellow pathways), which tend to prevent redundant connections  $\mathcal{L}$  in the nonwetting phase (NWP). Cluster growth of the wetting phase during imbibition is initiated through snap-off events (yellow) which gradually merge into compact wetting clusters that tend to preserve redundant connections in the remaining NWP clusters. (b) Nonwetting phase during primary drainage (left) and main imbibition (right) in the investigated region of interest (ROI). Apparently disconnected NWP clusters are connected through external pathways that are not captured by the ROI. (c) Shape of the 3-D fluid interfaces in a subvolume of  $10\text{mm}^3$  for primary drainage (left) and main imbibition (right) at roughly the same  $S_w$ . The wetting phase is depicted in blue and fluid interfaces in red. Note that during imbibition the wetting front does not traverse the subvolume from bottom to top but laterally because the bulk wetting phase expands from the center of the image as a compact cluster.

imbibition are depicted in Figure 1b. Movies of three-dimensional distribution of the nonwetting fluid during the entire experiment are available as supplementary information, Movies S1–S3.

The constitutive relationships between conventional, macroscopic state variables ( $P_c(S_w)$ ,  $A_{wn}(S_w)$ ) exhibit distinct hysteresis between drainage and imbibition (Figures 2a and 2b), whereas drainage curves for primary and main drainage are almost identical. This is because nonwetting phase (NWP) entrapment during imbibition is negligible in the investigated region of interest (ROI). The only difference between primary and main drainage is a slightly lower entry pressure for main drainage (Figure 2a). This is caused by irreducible nonwetting fluid outside of the ROI at the end of imbibition which enters the ROI more readily during MD [Reeves and Celia, 1996]. Interfacial area  $A_{wn}$  also exhibits distinct hysteresis (Figure 2b), with lower interface densities during imbibition. Polynomial fits to the constitutive relationships between all three state variables ( $P_c$ ,  $S_w$ ,  $A_{wn}$ ) are presented in supporting information, S3. In line with Joekar-Niasar et al. [2008] and Porter et al. [2010], the  $A_{wn}(S_w, P_c)$ -relationship including both drainage and imbibition is approximated well with a biquadratic polynomial fit.

Visual observation clearly shows that different shapes of fluid interfaces for reversed pump directions are the cause for the  $A_{wn}(S_w)$  hysteresis (Figure 1c). During drainage, the NWP forms fingers which are typical for an invasion percolation process. During imbibition a single, compact wetting phase cluster with a rather flat surface expands from the center of the sample which causes a lower interfacial area.

In the following, it will be argued that fluid topology provides a more thorough description of these different pore-scale fluid configurations than fluid interface density. During drainage,  $\chi_n$  is initially slightly positive as the nonwetting phase invades the sample from several, apparently disconnected locations (Figure 2c); an artifact of the limited field of view. Then  $\chi_n$  turns negative at  $S_w \approx 0.6$ , i.e., the NWP has merged into one connected cluster. As more pore bodies get drained, the number of redundant loops in the NWP around grains and brine menisci increases which leads to further reduction of  $\chi_n$ . The decrease is nonlinear, because the chance that a random Haines jump [Haines, 1930], i.e., an interfacial jump from one pore constriction to another, generates new loops in the NWP is higher at low saturation. That is because the chance that adjacent pore bodies are already drained is higher at low  $S_w$ . In contrast, the increase in  $\chi_n$  with increasing  $S_w$  during imbibition is almost linear. This suggests that the order in which brine reenters the pore space is characteristically different from the order in which it was drained (Figure 1c). During imbibition, the wetting phase did not invade the sample randomly. The first pore bodies that got reinvaded are located in the center of the sample and the wetting front started to grow from there as a rather compact

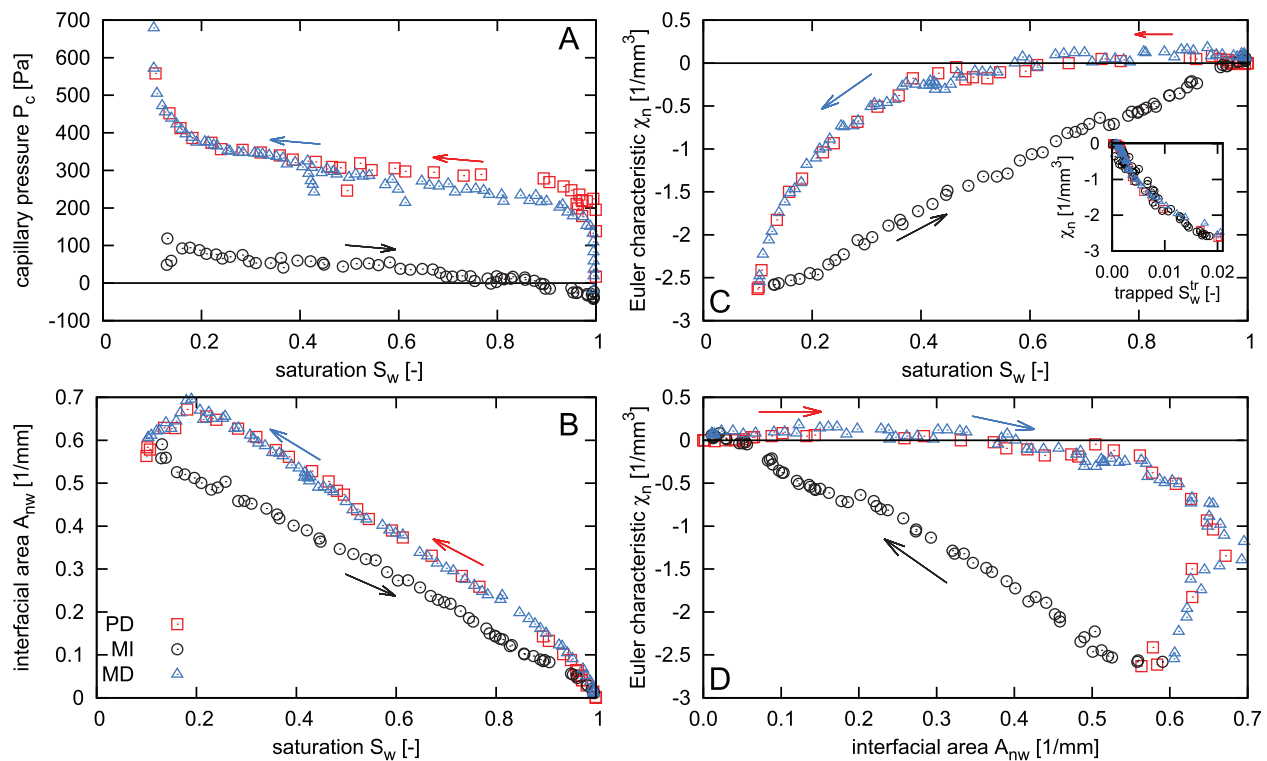


**Figure 2.** Capillary pressure  $P_c$  (a) and interfacial area  $A_{nw}$  (b) and Euler characteristic (c) as a function of saturation  $S_w$  during primary drainage (PD), main imbibition (MI), and main drainage (MD) for the region of interest (ROI) depicted in Figure 1b. The inset shows the linear relationship between  $\chi_n$  and the wetting fluid trapped in pendular rings  $S_w^{tr}$ . The Euler characteristic is also plotted as a function of interface density (D) to demonstrate the hysteretic behavior of both state variables.

cluster. In this way, many redundant loops in the NWP further away from the compact wetting cluster are preserved. They are only disrupted gradually by growth of the wetting cluster as imbibition proceeds. Interestingly, this  $\chi_n$  hysteresis disappears, when bulk saturation  $S_w$  is substituted by trapped wetting phase saturation  $S_w^{tr}$ . Hence, there is a causal link between the number of redundant loops in the NWP and wetting phase trapping in isolated pendular rings (Figure 2c, inset). That is, the more pore constrictions are invaded by the NWP the more wetting fluid is trapped in isolated pendular rings at grain contacts. This interdependency will be further discussed below. Note that none of the other state variables ( $S_w$ ,  $A_{wn}$ ,  $\chi_w$ ) exhibits a such a unique relationship with  $S_w^{tr}$  (supporting information, **S4**).

The hysteresis in the  $\chi_n(A_{wn})$ -relationship implies that the topology of the nonwetting fluid carries complementary information that cannot be described by fluid interface density alone (Figure 2d). Interestingly, the joint  $A_{wn}(S_w, \chi_n)$ -relationship (supporting information, **S3**) is bilinear, i.e., it simplifies to a hyperplane in the feature space. This level of consistency is remarkable. Presumably the pore space is too small or too regular to evoke a wealth of pore-scale fluid configurations that departs from this plane. The Euler characteristic for the wetting phase  $\chi_w$  is explained in supporting information, **S5**. Also  $\chi_w(S_w)$  exhibits distinct hysteresis which can again be attributed to different patterns of the displacement front during drainage and imbibition. In contrast to the nonwetting phase, a quantitative analysis of the wetting phase topology is much more dependent on image resolution and segmentation quality because of thin wetting films close to the resolution limit. Furthermore  $\chi_w(S_w)$  are not monotonic which hampers a scaling analysis as introduced below. For these reasons, our main focus will be limited to NWP topology.

### 3.2. Fractional Flow in a Complex Porous Medium

Sintered glass beads represent a simplified porous medium that does not capture the complexity of natural rock. The bead surfaces are smooth and the aspect ratio between pore bodies and pore constrictions is small. As a consequence, fluid displacement is mainly reversible and the volume work done on the system is mostly transformed into surface energy [Morrow, 1970; Seth et al., 2007]. A unique  $P_c(A_{wn}, S_w)$ -relationship is more likely to exist under these conditions as the fluid configurations depend on the displacement

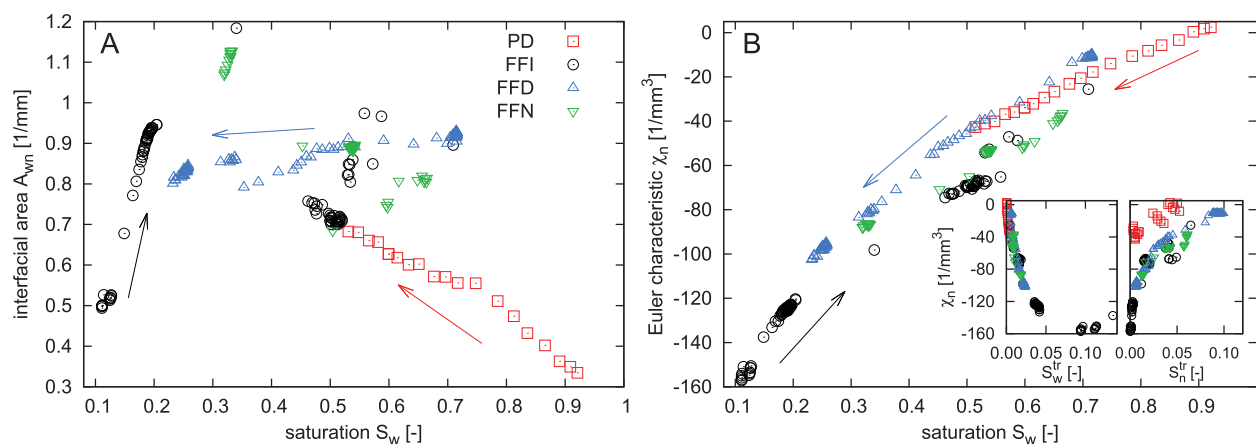


**Figure 3.** Interfacial area  $A_{wn}$  (a) and Euler characteristic of the nonwetting phase  $\chi_n$  (b) as a function of saturation  $S_w$  for a sequence of fractional flow rates, where both fluids are pumped into the sample simultaneously and the assignment to either drainage (FFD), imbibition (FFI), or neutral (FFN) is done according to the net change in saturation. Initially the sample was completely saturated ( $S_w = 1$ ). The primary drainage (PD) that initiated the fractional flow experiment is reported separately. In the insets total  $S_w$  is either replaced by trapped wetting fluid  $S_w^{tr}$  or trapped nonwetting fluid  $S_w^{nr}$ .

process alone. Sandstone and carbonate rock in turn exhibit rough grain surfaces and higher aspect ratios that lead to an increase in irreversible displacement via Haines jumps and snap-off which transform volume work into heat dissipation. In this way, the net efficiency, i.e., the proportion of total work routed into surface energy, decreases from 85% for random sphere packings to 20–40% for natural rock [Seth *et al.*, 2007; Berg *et al.*, 2013]. The fluid configurations are more likely to be governed by pinned interfaces and random displacement events. This raises the question whether the hitherto observed, simplified relationships between fluid topology and conventional macroscopic state variables only hold for reversible displacement. We tested this by analyzing a fractional flow experiment in a sintered Robuglas<sup>®</sup> sample with better resemblance of a natural rock [Rücker *et al.*, 2015a].

The  $A_{wn}(S_w, \chi_n)$ -relationship still roughly follows a bilinear trend, but is indeed more scattered around the hyperplane with systematic deviations depending on the displacement process (supporting information, S3). The scatter stems from variation in interfacial area. When two-phase flow is governed by irreversible displacement,  $A_{wn}$  does not only depend on the flow regime but also on the phase distribution of the receding fluid and hence on the entire history of the system.

The two-dimensional projections of the data into the  $A_{wn}(S_w)$  (Figure 3a) and  $\chi_n(S_w)$  space (Figure 3b) provides some insights into the origin of the  $A_{wn}(S_w, \chi_n)$  hysteresis. The hysteresis in interfacial area is qualitatively different from the hysteresis in NWP fluid topology. For instance, in the same saturation range around  $S_w = [0.5; 0.7]$   $A_{wn}$  may either increase (PD) or decrease (FFD) during drainage depending on how the receding wetting fluid is distributed in the pore space. Hence, the interface density at a given point in time depends on the entire history of fluid displacement up to this point. If the flow is dominated by irreversible displacement through Haines jumps and snap-off, then the chances to return to a similar fluid configurations reduces drastically. The trajectories of interfacial area then become virtually unpredictable especially at intermediate saturation when both fluids are mobile. The Euler characteristic of the NWP, in turn, seems to behave in a much more predictable way. The change in  $\chi_n$  strictly depends on the net change in  $S_w$  and much less on the phase distribution in the pore space. As a consequence, the primary drainage and secondary drainage during fractional flow align on the same curve. The  $\chi_n(S_w)$  hysteresis implies that during drainage NWP ganglia have a more finger-like shape that avoids loops around grains. During imbibition, in turn, the NWP loops that do exist around grains are maintained for a while when  $S_w$  increases and are only gradually removed through snap-off at pore constrictions everywhere in the sample [Rücker *et al.*, 2015b]. More importantly, for irreversible ganglion dynamics during fractional flow, the only cause for hysteresis seems to be a difference in the rates of  $\chi_n$  change due to different pore scale mechanisms that prevail during drainage and imbibition and not the history of the system. This is a remarkable finding, as it allows us to identify complex displacement patterns with a single curve. For this reason, the  $\chi_n(S_w)$  relationship lends itself to a process-dependent power-law scaling.

Interestingly, the hysteresis in the NWP topology vanishes when the total  $S_w$  is replaced by the saturation of trapped wetting fluid,  $S_w^{tr}$  (Figure 3b, inset). Conversely,  $\chi_n$  as a function of trapped nonwetting fluid saturation,  $S_n^{tr}$ , conserves a small hysteresis between drainage and imbibition and even reveals a difference between primary drainage and fractional drainage (supporting information Figure S3b, inset). The low amount of NWP trapping during PD is obviously due to fact that the pore space needs to be filled with the nonwetting fluid first before a considerable amount of snap-off at pore constrictions can occur. The higher amount of scatter in the  $S_n^{tr}$  data is likely to be caused by a limited sample size. Trapped nonwetting phase clusters on average are bigger than trapped wetting phase clusters. Ganglia of the nonwetting phase often comprise several adjacent pore bodies and the biggest clusters may reach the size of the field of view so that the amount of NWP trapping is underestimated [Armstrong *et al.*, 2014]. The relationship between fluid trapping ( $S_w^{tr}$ ,  $S_n^{tr}$ ) and other state variables ( $S_w$ ,  $A_{wn}$ ,  $\chi_w$ ) is provided as supporting information, **S4**.

## 4. Discussion

### 4.1. Power-Law Scaling of the Euler Characteristic

The analysis of both experiments indicates that (i) the Euler characteristic  $\chi_n$  is a suitable measure for displacement patterns and that (ii) its change with changing saturation is process-dependent. As a result, drainage and imbibition exhibit different  $\chi_n(S_w)$  curves. In the following, we will establish that the underlying displacement mechanisms can in fact be deduced from the shape of the  $\chi_n(S_n)$  curve, where  $S_n = 1 - S_w$ . To do so, we take advantage of a normalized Euler characteristic of the nonwetting phase  $\hat{\chi}_n$  that has recently been introduced as a means to describe the effect of fluid topology on NWP trapping [Herring *et al.*, 2013, 2015]. Normalization is achieved by dividing the saturation-dependent  $\chi_n$  by the Euler characteristic of the entire pore space, so that  $\hat{\chi}_n$  reaches unity at full NWP saturation. To the best of our knowledge, we present the first demonstration that  $\hat{\chi}_n$  as a function of  $S_n$  strictly follows a power law relation of the form

$$\hat{\chi}_n = pS_n^k + \epsilon \quad (2)$$

where  $k$  is characteristic for the slope of  $\hat{\chi}_n$  as a function of NWP saturation  $S_n$  and  $p, \epsilon$  are additional, free parameters. Equation (2) is fitted to the data across the entire saturation range via least squares minimization. The exponent  $k$  turns out to be characteristic for the flow regime and independent of the underlying porous medium.

The importance of NWP topology for imbibition has been stressed early on [Lenormand *et al.*, 1983; Wardlaw and Yu, 1988; Hughes and Blunt, 2000]. For micromodels of regular ducts, it was defined locally at the wetting front as the number of adjacent ducts filled with nonwetting fluid, e.g., in a range from one to three in a two-dimensional square lattice. We observed cluster growth during imbibition in the quasistatic experiment which is typical for a combination of slow imbibition and reduced wettability [Hughes and Blunt, 2000] with some initial wetting phase saturation prior to rewetting [Wardlaw and Yu, 1988]. In this type of mechanism, the chances of pore filling decreases with the number of adjacent ducts still filled with nonwetting fluid. This leads to the expansion of a compact cluster for which the remaining NWP-filled pore space further away from the cluster stays intact and maintains its high connectivity (cf. Figure 1a). In this way, the reduction of loops in the nonwetting phase merely scales linearly with the reduction in  $S_n$  as the wetting cluster grows, which leads to a power law exponent  $k$  close to one. This is true for main imbibition in the quasistatic experiment ( $k = 1.10$  in Figure 4a).

Slow drainage as investigated in the quasistatic experiment is known to evoke an invasion-percolation type of drainage pattern, which is independent of fluid topology, but heavily dependent on pore sizes and aspect ratios [Lenormand *et al.*, 1988; Blunt and Scher, 1995]. The formation of an invading NWP finger leads to an increase in  $S_n$  but does not have an effect on  $\hat{\chi}_n$  per se. This normalized Euler characteristic only increases if a NWP loop is formed around a grain or if the tip of the finger reconnects with the nonwetting phase elsewhere (cf. Figure 1a). In a hypothetical case of self-avoiding fingers with the thickness of only one pore body, redundant loops would be prevented up to very high  $S_n$  so that  $\hat{\chi}_n$  remains constant until eventually the self-avoidance breaks down everywhere at once, leading to a sudden increase in  $\hat{\chi}_n$  and thus to a very high  $k$ . Real drainage patterns of course exhibit irregular fronts and fingers of a certain thickness leading to loops around grains within wider fingers. Also, realistic branching patterns continuously lead to

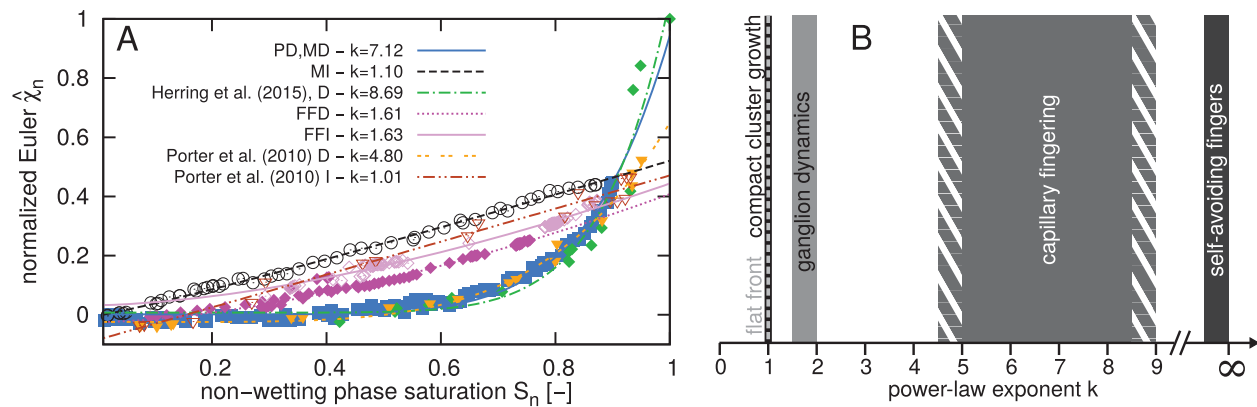


**Figure 4.** (a) Normalized Euler characteristic  $\hat{\chi}_n$  as a function of nonwetting phase saturation or different synchrotron experiments. The fitted lines correspond to a power law function of the form  $\hat{\chi}_n = pS_n^k + \epsilon$  with  $p, k, \epsilon$  as free parameters for various drainage (filled symbols) and imbibition experiments (empty symbols). (b) Range of observed scaling exponents in the investigated flow experiments and modeled fluid distributions (discussed in supporting information, **S6**) and its classification into various fluid displacement mechanisms.

random reconnection of the nonwetting phase through Haines jumps. As mentioned earlier, the slope of  $\hat{\chi}_n$  for invasion percolation tends to be nonlinear since the chance that a Haines jumps creates one or many new redundant loops in the NWP increases with increasing  $S_n$ . This is because the probability of pores in the neighborhood to already be filled by NWP is higher at high  $S_n$ . This nonlinearity is expressed by a high-scaling exponent of  $k = 7.12$ .

The results from the fractional flow experiment are analyzed separately for drainage (FFD) and imbibition (FFI) depending on the net change in saturation. That is, for FFD the pore volume invaded by the nonwetting phase exceeds the pore volume from which the NWP recedes, and vice versa. The slope of both curves is similar with scaling parameters ( $k = 1.61, 1.63$ ) that are smaller than those observed for invasion percolation during quasistatic drainage, but higher than that observed for compact expansion of the wetting front during quasistatic imbibition. The hysteresis is small but consistent with the other experiments.

We expect the power law exponent  $k$  to be mainly dependent on the displacement process and less on the pore space architecture. To test this, we also show data from various other synchrotron experiments (Figure 4a) and simulated flow experiments (supporting information, **S6**). Information about all datasets is summarized in Table 1. A rough classification of observed exponents into governing flow regimes is presented in Figure 4b. The experimental data by Porter et al. [2010] was obtained with a similar glass bead sample. Also the fluids (brine and Soltrol) and flow rates were similar to our study. A distinct hysteresis in  $\hat{\chi}_n$  is again evident between imbibition ( $k = 1.01$ ) and drainage ( $k = 4.80$ ). NWP entrapment occurs at very low  $S_n$ , which is indicated by  $\hat{\chi}_n < 0$ . The data by Herring et al. [2015] were obtained for repeated drainage of two Bentheimer sandstone samples (brine and air). Every data point was obtained for a new drainage process starting again at full brine saturation. In spite of a completely different drainage history and pore space

**Table 1.** Summary of Fitting Parameters ( $p, k, \epsilon$ ) and Coefficient of Determination ( $R^2$ ) for the Scaling Behavior of the Normalized Euler Characteristic  $\hat{\chi}_n$  (Equation (2))<sup>a</sup>

Data Set	Porous Medium	$\chi_0$ (mm <sup>-3</sup> )	Flow Regime	Flow Direction	p	k	$\epsilon$	$R^2$
PD, MD	Glass beads	-5.87	Capillary fingering	Drainage	0.94	7.12	0.002	1.000
MP					1.97	5.01	-0.003	0.997
MI			Cluster growth	Imbibition	0.52	1.10	-0.006	0.999
FFD	Robuglas <sup>®</sup>	-407	Ganglion dynamics	Drainage	0.43	1.61	-0.025	0.981
FFI				Imbibition	0.41	1.63	0.033	0.981
FF, front			Sharp front		0.99	1.00	-0.006	0.997
Herring et al. [2015]	Sandstone	-302, -367	Capillary fingering	Drainage	1.06	8.69	0.007	0.922
Herring et al. [2015], MP					1.02	5.98	-0.015	0.997
Porter et al. [2010], D	Glass beads	-4.66	Capillary fingering	Drainage	0.67	4.80	-0.025	1.000
Porter et al. [2010], I			Cluster growth	Imbibition	0.56	1.01	-0.084	1.000

<sup>a</sup>In addition, the Euler characteristic of the pore space  $\chi_0$  is reported for each investigated porous medium. Name of data set is according to Figure 4 and the model results presented as supporting information (MP; FF, front; and Herring et al. [2015], MP in **S6**).

architecture with lower porosity, smaller mean pore diameter and more angular grain surfaces we observe very similar  $\hat{\chi}_n$  curves and power law exponents  $k$ . These findings are corroborated by simplified, modeled fluid distributions using the same, image-derived pore space architectures (supporting information, **S6**). There it is demonstrated that simulated capillary fingering leads to  $k > 5$  irrespective of the underlying pore structure. The broad range of  $k = [4.8; 8.7]$  for all experimental and simulated capillary fingering data is probably a result of different mobility ratios and capillary numbers, which ultimately governs the strength of fingering [Lenormand *et al.*, 1988]. Flat frontal displacement as simulated with piston flow in the absence of capillarity leads to  $k = 1$  similar to cluster growth.

In summary, the power-law exponent  $k$  is representative of the underlying displacement process and carries integrated information about the regularity of the imbibition and drainage front over the entire saturation range including trapping efficiency at low saturation. Thus,  $k$  has distinct advantages over other morphological descriptors, like finger width [Weitz *et al.*, 1987; Blunt and Scher, 1995], since the latter can be ill-defined depending on the specific process. Moreover, the choice of the Euler characteristic to describe fluid configurations is not arbitrary but motivated by integral geometry. Unlike thermodynamic capillary pressure hysteresis models [Hassanizadeh and Gray, 1993; Gray and Miller, 2005], integral geometry makes no a priori assumptions about the continuity of phases but rather assesses this continuity directly by putting fluid topology into focus as one of the key metrics to describe complex structures. Though not yet fully understood, this new perspective is beneficial in several ways: (i) Unlike interfacial area  $A_{wn}$ , NWP topology  $\chi_n$  as a function of saturation seems to be only governed by the underlying displacement process and not by the history of the system. (ii) While many displacement patterns can lead to the same interfacial area at equal saturation they cannot at the same time have equal Euler characteristics (cf. Figure 1a). In turn, if one fluid is displaced by another through a single displacement mechanism, then the morphology of the front governs how fluids are disrupted and the loops around the solid phase are formed or destroyed. This results in a characteristic change in the Euler characteristic of the nonwetting phase as interfaces move, which eventually leads to the observed power-law behavior of  $\hat{\chi}_n$ . (iii) NWP topology exhibits a nonhysteretic relationship with wetting fluid trapping and to a lesser degree also with nonwetting fluid trapping. This will be discussed below from a mathematical perspective. From a phenomenological perspective, this simply means that the more redundant loops of the NWP exist, the higher the chance for the wetting phase to be trapped in ganglia or pendular rings around grain contacts [Herring *et al.*, 2015]. Note that the wetting phase might still be connected through films smaller than the resolution limit. Neither, conventional state variables ( $S_w$ ,  $A_{wn}$ ) nor the Euler characteristic of the wetting phase ( $\chi_w$ ) exhibit a similar degree of uniqueness as a function of trapped fluid phases (supporting information, **S4**). More experiments in complex natural rocks like sandstone and limestone under different flow regimes will soon be available to check the general validity of all three abovementioned observations.

#### 4.2. Relevance for Flow and Transport

Hysteresis in the constitutive relationships between state variables at equilibrium usually implies that an important state variable is ignored. This shortcoming has been addressed along two different lines. In an engineering context, hysteresis is usually accounted for by empirical extensions to the constitutive  $P_c(S_w)$ -relationship that either address the difference between drainage and imbibition [Mualem, 1974; Kool and Parker, 1987] or dynamic effects [Barenblatt *et al.*, 2003; Hassanizadeh *et al.*, 2002; Mitkov *et al.*, 1998]. The question of a missing state variable is not addressed and the additional parameters may again be nonunique and depend on the state of the system. In a physical context, the focus is instead on the identification of the missing state variables. Given the importance of fluid topology as an independent state variable, the ultimate goal is of course to extend constitutive theories of macroscopic two-phase flow accordingly. The Euler characteristic is a topological invariant, which is generally accepted to characterize the connectivity of spatial structures [Mecke and Arns, 2005], based not only on the connectivity of simplicial complexes, but also on certain numerical proximities to percolation thresholds [Mecke and Wagner, 1991; Mecke, 2000; Vogel *et al.*, 2010]. According to these arguments,  $\chi$  should be one of the most important quantities, because transport and fluid flow in porous media are controlled by connectivity. In fact, because connectivity controls flow for immiscible displacement, the distinction between percolating and nonpercolating fluid phases was introduced into two-phase flow theories [Hilfer, 1998, 2006]. The basic physical idea in these publications rested on experimental observations in micromodels showing that percolating and nonpercolating fluid clusters respond differently to applied pressure gradients [Avraam and Payatakes, 1995]. Hysteresis of

fluid displacement results from breakup and coalescence of fluid clusters. The pore-scale processes of breakup and coalescence were represented macroscopically as mass transfer terms analogous to chemical reactions [Hilfer, 1998, 2006]. The Euler characteristic  $\chi$ , however, was conspicuously absent from the constitutive laws.

Our experimental findings (Figures 2c and 3) demonstrated a nonhysteretic relationship between  $\chi_n$  and nonpercolating  $S_w^{tr}$ , and to a lesser degree also with  $S_w^{tr}$ , that is independent of the underlying displacement process and the complexity of the pore space. The strong correlation between these entities suggests a causal link between the amount of trapped wetting clusters in pore constrictions and the amount of redundant pore connections occupied by the nonwetting fluid. In supporting information, **S7**, we discuss in more detail the mathematical link between percolation, as defined in Hilfer [1998, 2006], and simplicial connectivity, as defined and measured by the Euler characteristic  $\chi$  [Mecke, 2000; Mecke and Arns, 2005; Vogel et al., 2010]. This link via emerging clusters of a phase can only be an indirect relation because the Euler characteristic is local and additive, while the percolation property is nonlocal and nonadditive [Hilfer, 2000, 2002].

In summary, information about microscale fluid configurations needs to be reduced into a few macroscale parameters during upscaling of flow and transport to the Darcy scale [Gray and Miller, 2005]. Ideally, only information that is not relevant for macroscopic flow behavior gets lost. Here we outlined the relevance of fluid connectivity in macroscopic flow equations, either expressed through nonwetting fluid topology or related measures of connected and trapped fluid saturations. Ultimately, this may provide a means to incorporate the impact of flow regimes on effective Darcy-scale flow behavior in porous media.

## 5. Conclusions and Outlook

Fast, synchrotron-based X-ray tomography is currently being developed at a striking pace and with it comes the unique opportunity to track moving fluid interfaces during immiscible flow in natural, porous media in real time. Using this method, we have demonstrated that fluid topology, i.e., the way a fluid phase is linked through redundant connections, is characteristic for the underlying displacement pattern. Moreover, fluid topology correlates well with percolation properties and also helps to explain hysteresis effects that are typically observed for the constitutive relationships between macroscopic state variables.

Our findings raise some questions, which have to be addressed in future studies. (i) The suitability of the Euler characteristic in describing hysteresis of relative permeability has to be investigated. While an effect of fluid connectivity on relative permeability is very likely, it is hard to analyze this under realistic conditions. A viable, but time-consuming option would be Navier-Stokes simulations on static fluid distributions obtained from X-ray tomography. While these estimates result in reasonable values for connected pathway flow, the method fails completely in predicting the contribution from mobilized ganglia [Berg et al., 2016]. (ii) The presented fluid topology scaling analysis provides a new approach to evaluate effective process behavior, like trapping efficiency of CO<sub>2</sub> or oil production through water flooding, via image analysis. Furthermore it provides a formidable tool to test the ability of Navier-Stokes solvers and other computational methods in the emerging field of digital rock physics to reproduce the observed fluid displacement patterns in porous media. Future experiments and numerical simulations will help to populate entire phase diagrams of flow regimes for different forces balances [Lenormand et al., 1988] with corresponding scaling exponents. In this way, a hitherto qualitative description of systematic trends in changing front morphology is substituted by a quantitative analysis.

## References

- Armstrong, R. T., A. Georgiadis, H. Ott, D. Klemin, and S. Berg (2014), Critical capillary number: Desaturation studied with fast X-ray computed microtomography, *Geophys. Res. Lett.*, *41*, 55–60, doi:10.1002/2013GL058075.
- Avraam, D. G., and A. C. Payatakes (1995), Flow regimes and relative permeabilities during steady-state two-phase flow in porous media, *J. Fluid Mech.*, *293*, 207–236, doi:10.1017/S0022112095001698.
- Barenblatt, G., T. Patzek, and D. Silin (2003), The mathematical model of nonequilibrium effects in water-oil displacement, *SPE J.*, *8*(4), SPE-87329-PA, doi:10.2118/87329-PA.
- Bear, J. (1972), *Dynamic of Fluids in Porous Media*, Elsevier, N. Y.
- Berg, S., et al. (2013), Real-time 3D imaging of Haines jumps in porous media flow, *Proc. Natl. Acad. Sci. U. S. A.*, *110*(10), 3755–3759, doi:10.1073/pnas.1221373110.
- Berg, S., et al. (2014), Multiphase flow in porous rock imaged under dynamic flow conditions with fast X-ray computed microtomography, *Petrophysics*, *55*(4), 304–312.

### Acknowledgments

This research used resources of the Advanced Photon Source which is a DOE Office of Science User Facility operated for the DOE Office of Science by Argonne National Laboratory under Contract DE-AC02-06CH11357. We acknowledge the support of GeoSoilEnviroCARS (Sector 13), which is supported by the National Science Foundation Earth Sciences (EAR-1128799), and the Department of Energy, Geosciences (DE-FG02-94ER14466). This research was supported by the US National Science Foundation, award # EAR-1344877. We thank Mark Rivers at the Advanced Photon Source for assistance at the GSECARS beam line, Holger Ott and Apostolos Georgiadis (Shell) for assistance during the fractional flow experiment, as well as Anna Herring and Tianyi Li (OSU) for proving data. The first author is grateful to the Alexander-von-Humboldt Foundation for granting a Feodor-von-Lynen scholarship. Rudolf Hilfer thanks the Deutsche Forschungsgemeinschaft for financial support. Access to tools used for image processing is provided as supporting information. Images are available from the authors upon request.

- Berg, S., et al. (2016), Connected pathway relative permeability from pore-scale imaging of imbibition, *Adv. Water Resour.*, 90, 24–35, doi:10.1016/j.advwatres.2016.01.010.
- Blunt, M. J., and H. Scher (1995), Pore-level modeling of wetting, *Phys. Rev. E*, 52, 6387–6403, doi:10.1103/PhysRevE.52.6387.
- Dullien, F. (1992), *Porous Media: Fluid Transport and Pore Structure*, Academic Press, N. Y.
- Gray, W. G., and C. T. Miller (2005), Thermodynamically constrained averaging theory approach for modeling flow and transport phenomena in porous medium systems: 1. Motivation and overview, *Adv. Water Resour.*, 28(2), 161–180, doi:10.1016/j.advwatres.2004.09.005.
- Hadwiger, H. (1957), *Vorlesungen über Inhalt, Oberfläche und Isoperimetrie (Lecture on Content, Surface and Isoperimetry)*, 312 pp., Springer-Verlag, Berlin-Heidelberg.
- Haines, W. (1930), Studies in the physical properties of soil. V. The hysteresis effect in capillary properties, and the modes of moisture distribution associated therewith, *J. Agric. Sci.*, 20, 97–116, doi:10.1017/S002185960008864X.
- Hassanizadeh, S., and W. Gray (1993), Thermodynamic basis of capillary pressure in porous media, *Water Resour. Res.*, 29(10), 3389–3405.
- Hassanizadeh, S., M. Celia, and H. Dahle (2002), Dynamic effect in the capillary pressure–saturation relationship and its impacts on unsaturated flow, *Vadose Zone J.*, 1(1), 38–57.
- Herring, A. L., E. J. Harper, L. Andersson, A. Sheppard, B. K. Bay, and D. Wildenschild (2013), Effect of fluid topology on residual nonwetting phase trapping: Implications for geologic CO<sub>2</sub> sequestration, *Adv. Water Resour.*, 62(Part A), 47–58.
- Herring, A. L., L. Andersson, S. Schlüter, A. Sheppard, and D. Wildenschild (2015), Efficiently engineering pore-scale processes: The role of force dominance and topology during nonwetting phase trapping in porous media, *Adv. Water Resour.*, 79, 91–102, doi:10.1016/j.advwatres.2015.02.005.
- Hilfer, R. (1998), Macroscopic equations of motion for two-phase flow in porous media, *Phys. Rev. E*, 58, 2090–2096, doi:10.1103/PhysRevE.58.2090.
- Hilfer, R. (2000), Local porosity theory and stochastic reconstruction for porous media, in *Räumliche Statistik und Statistische Physik, Lecture Notes in Physics*, vol. 554, edited by D. Stoyan and K. Mecke, p. 203, Springer, Berlin.
- Hilfer, R. (2002), Review on scale dependent characterization of the microstructure of porous media, *Transp. Porous Media*, 46, 373–390.
- Hilfer, R. (2006), Macroscopic capillarity and hysteresis for flow in porous media, *Phys. Rev. E*, 73, 016,307, doi:10.1103/PhysRevE.73.016307.
- Hilfer, R., and H. Besserer (2000), Macroscopic two-phase flow in porous media, *Physica B*, 279(1–3), 125–129, doi:10.1016/S0921-4526(99)00694-8.
- Hilfer, R., and P. Øren (1996), Dimensional analysis of pore scale and field scale immiscible displacement, *Transp. Porous Media*, 22(1), 53–72, doi:10.1007/BF00974311.
- Hughes, R. G., and M. J. Blunt (2000), Pore scale modeling of rate effects in imbibition, *Transp. Porous Media*, 40(3), 295–322, doi:10.1023/A:1006629019153.
- Joekar-Niasar, V., and S. Hassanizadeh (2012), Uniqueness of specific interfacial area–capillary pressure–saturation relationship under non-equilibrium conditions in two-phase porous media flow, *Transp. Porous Media*, 94(2), 465–486, doi:10.1007/s11242-012-9958-3.
- Joekar-Niasar, V., S. Hassanizadeh, and A. Leijnse (2008), Insights into the relationships among capillary pressure, saturation, interfacial area and relative permeability using pore-network modeling, *Transp. Porous Media*, 74(2), 201–219.
- Karadimitriou, N. K., S. M. Hassanizadeh, V. Joekar-Niasar, and P. J. Kleingeld (2014), Micromodel study of two-phase flow under transient conditions: Quantifying effects of specific interfacial area, *Water Resour. Res.*, 50, 8125–8140, doi:10.1002/2014WR015388.
- Kool, J. B., and J. C. Parker (1987), Development and evaluation of closed-form expressions for hysteretic soil hydraulic properties, *Water Resour. Res.*, 23(1), 105–114.
- Krummel, A. T., S. S. Datta, S. Münster, and D. A. Weitz (2013), Visualizing multiphase flow and trapped fluid configurations in a model three-dimensional porous medium, *AIChE J.*, 59(3), 1022–1029, doi:10.1002/aic.14005.
- Lehmann, P., M. Berchthold, B. Ahrenholz, J. Tölke, A. Kaestner, M. Krafczyk, H. Fühler, and H. Künsch (2008), Impact of geometrical properties on permeability and fluid phase distribution in porous media, *Adv. Water Resour.*, 31, 1188–1204.
- Lenormand, R., C. Zarcone, and A. Sarr (1983), Mechanisms of the displacement of one fluid by another in a network of capillary ducts, *J. Fluid Mech.*, 135, 337–353, doi:10.1017/S0022112083003110.
- Lenormand, R., E. Touboul, and C. Zarcone (1988), Numerical models and experiments on immiscible displacements in porous media, *J. Fluid Mech.*, 189, 165–187, doi:10.1017/S0022112088000953.
- Marle, C. (1982), On macroscopic equations governing multiphase flow with diffusion and chemical reactions in porous media, *Int. J. Eng. Sci.*, 20(5), 643–662, doi:10.1016/0020-7225(82)90118-5.
- Mecke, K. (2000), Chapter 6: Additivity, convexity and beyond: Application of Minkowski functionals in statistical physics, in *Statistical Physics and Spatial Statistics: The Art of Analyzing and Modeling Spatial Structures and Pattern Formation, Lecture Notes in Physics*, vol. 554, edited by K. R. Mecke and D. Stoyan, LNP 554, pp. 111–184, Springer-Verlag, Berlin Heidelberg.
- Mecke, K., and C. H. Arns (2005), Fluids in porous media: A morphometric approach, *J. Phys. Condens. Matter*, 17(9), S503.
- Mecke, K., and H. Wagner (1991), Euler characteristic and related measures for random geometric sets, *J. Stat. Mech.*, 64, 843–850.
- Mitkov, I., D. M. Tartakovsky, and C. Larrabee Winter (1998), Dynamics of wetting fronts in porous media, *Phys. Rev. E*, 58, R5245–R5248, doi:10.1103/PhysRevE.58.R5245.
- Morrow, N. R. (1970), Physics and thermodynamics of capillary action in porous media, *Ind. Eng. Chem.*, 62(6), 32–56, doi:10.1021/ie50726a006.
- Muallem, Y. (1974), A conceptual model of hysteresis, *Water Resour. Res.*, 10(3), 514–520, doi:10.1029/WR010i003p00514.
- Niessner, J., and S. M. Hassanizadeh (2008), A model for two-phase flow in porous media including fluid-fluid interfacial area, *Water Resour. Res.*, 44, W08439, doi:10.1029/2007WR006721.
- Ohser, J., and P. Mücklich (2000), *Statistical Analysis of Microstructures in Material Science*, John Wiley, N. Y.
- Pak, T., I. B. Butler, S. Geiger, M. I. J. van Dijke, and K. S. Sorbie (2015), Droplet fragmentation: 3D imaging of a previously unidentified pore-scale process during multiphase flow in porous media, *Proc. Natl. Acad. Sci. U. S. A.*, 112(7), 1947–1952, doi:10.1073/pnas.1420202112.
- Porter, M., D. Wildenschild, G. Grant, and J. Gerhard (2010), Measurement and prediction of the relationship between capillary pressure, saturation, and interfacial area in a NAPL-water-glass bead system, *Water Resour. Res.*, 46, W08512, doi:10.1029/2009WR007786.
- Reeves, P., and M. Celia (1996), A functional relationship between capillary pressure, saturation, and interfacial area as revealed by a pore-scale network model, *Water Resour. Res.*, 32(8), 2345–2358.
- Rücker, M., et al. (2015a), From connected pathway flow to ganglion dynamics, *Geophys. Res. Lett.*, 42, 3888–3894, doi:10.1002/2015GL064007.

- Rücker, M., S. Berg, R. Armstrong, A. Georgiadis, H. Ott, L. Simon, F. Enzmann, M. Kersten, and S. De With (2015b), The fate of oil clusters during fractional flow: Trajectories in the saturation-capillary number space, in *Proceedings of the Society of Core Analysis, St. Johns, Canada, 2015*, Society of Core Analysts, Fredericton, New Brunswick E3B 0H8 Canada.
- Seth, S., et al. (2007), Efficiency of the conversion of work of drainage to surface energy for sandstone and carbonate, *SPE Reservoir Eval. Eng.*, 10(4), 338–347.
- Vogel, H.-J., U. Weller, and S. Schlüter (2010), Quantification of soil structure based on Minkowski functions, *Comput. Geosci.*, 36(10), 1236–1245, doi:10.1016/j.cageo.2010.03.007.
- Wardlaw, N. C., and L. Yu (1988), Fluid topology, pore size and aspect ratio during imbibition, *Transp. Porous Media*, 3(1), 17–34, doi: 10.1007/BF00222684.
- Weitz, D., J. Stokes, R. Ball, and A. Kushnick (1987), Dynamic capillary pressure in porous media: Origin of the viscous-fingering length scale, *Phys. Rev. Lett.*, 59(26), 2967–2970.